

Circa 180 Ma Ag-Bi-Pb-Mo-Cu-bearing quartz veins in a post-thrust calc-alkaline intrusion near Surprise Mountain, Iskut River area, northwestern British Columbia



K. Martin¹, A. Zagorevski^{2, a}, M.G. Mihalynuk³, N.L. Joyce², and R. Creaser⁴

¹ Department of Earth Sciences, University of Ottawa, Ottawa, ON, K1N 6N5

² Geological Survey of Canada, 601 Booth Street, Ottawa, ON, K1A 0E8

³ British Columbia Geological Survey, Ministry of Energy and Mines, Victoria, BC, V8W 9N3

⁴ Department of Earth and Atmospheric Sciences, University of Alberta, Edmonton, AB, T6G 2R3

^a corresponding author: alexandre.zagorevski@canada.ca

Recommended citation: Martin, K., Zagorevski, A., Mihalynuk, M.G., Joyce, N.L., and Creaser, R., 2016. Circa 180 Ma Ag-Bi-Pb-Mo-Cu-bearing quartz veins in a post-thrust calc-alkaline intrusion near Surprise Mountain, Iskut River area, northwestern British Columbia. In: Geological Fieldwork 2015, British Columbia Geological Survey Paper 2016-1, pp. 77-94.

Abstract

Polymetallic mineralized quartz veins are hosted by quartz diorite to quartz monzodiorite near Surprise Mountain, western Iskut River area. The intrusion is a homogeneous calc-alkaline, magnetite series granitoid that crosscuts an Early Jurassic thrust. New ⁴⁰Ar/³⁹Ar hornblende ages (178 ± 2 and 179 ± 2 Ma) from quartz diorite and a Re-Os molybdenite (180.2 ± 0.8 Ma) age from a mineralized quartz vein provide minimums for the time of pluton emplacement. Both age and composition suggest affiliation with the Cone Mountain plutonic suite. Polymetallic quartz veins contain pyrite, galena, and molybdenite; minor bismuthinite, covellite, chalcocite, chalcopyrite and pyrrotite; and traces of sphalerite. Geochemical analysis of veins reveals elevated Ag, Bi, Cu, Mo, Pb and Zn. Overall, the sporadic mineralization lacks clear horizontal metal zonation but may be related to polymetallic Ag-Pb-Zn±Au or Cu±Ag quartz deposit types, or may be peripheral to skarn or porphyry mineralization. Weak alteration, erratic and weak Au enrichment, and lack of metal zonation differentiates this occurrence from other Jurassic deposits in the area.

Keywords: Iskut River, Stikinia, Early Jurassic, Surprise Mountain, polymetallic vein, Cone Mountain plutonic suite

1. Introduction

Northern Stikinia (Fig. 1) has a rich and diverse metal endowment from a variety of mineral deposit types that reflect the varied tectonic history of the Canadian Cordillera. Deposits in northwestern Stikinia range from Mississippian volcanogenic massive sulphides to Triassic-Jurassic Cu-Au porphyry and Eocene epithermal vein systems (e.g., Logan and Koyanagi, 1994; Logan and Mihalynuk, 2014; Nelson and Kyba, 2014). The Late Triassic to early Middle Jurassic is one of the most important time intervals in the northern Cordillera, and is recorded by regionally extensive volcano-sedimentary rocks of the Hazelton Group (Tipper and Richards, 1976) and coeval plutons (Fig. 2). In the Iskut River region, the Hazelton Group exhibits a short but significant magmatic lull between ~185 and 178.5 Ma and an unconformity (Fig. 3; Lewis, 2013; Cutts et al., 2015). This magmatic lull marks the transition from porphyry and epithermal deposits formed during deposition of the lower part of the Hazelton Group and volcanogenic massive sulphide deposits in the upper part (e.g., Anderson and Thorkelson, 1990; Lewis, 2013; Nelson and Kyba, 2014; Kyba and Nelson, 2015). This magmatic lull is absent in the Telegraph Creek area, where the Cone Mountain plutonic suite was emplaced (Fig. 2; Brown et al., 1996). The duration and aerial extent of this magmatic gap and the distribution of Jurassic plutonic suites are important considerations for mineral exploration and for unravelling the tectonic history of Stikinia.

Herein we present field, petrographic, geochemical, and ⁴⁰Ar/³⁹Ar and Re-Os geochronologic data from a polymetallic quartz vein-bearing quartz diorite intrusion near Surprise Mountain in the western Iskut River area (Fig. 4), and relate the intrusion to the Cone Mountain suite. Our geochronologic data also show that a thrust fault juxtaposing Permian to Late Triassic marbles above Early Jurassic volcanoclastic rocks and cut by the Surprise Mountain intrusion was active during the magmatic lull.

2. Regional geology

The Iskut River area is along the western margin of the Stikine terrane in northwestern British Columbia (Figs. 1, 2). The oldest rocks in the area are part of the Stikine assemblage (Monger, 1977), which consists of Carboniferous bimodal arc magmatic rocks and Permian sedimentary strata. The Stikine assemblage is unconformably overlain by Triassic volcano-sedimentary rocks of the Stuhini Group; both are cut by the Stikine and Copper Mountain plutonic suites (e.g., Logan et al., 2000; Mihalynuk et al., 2012). Above a regional unconformity bevelled into these rocks are volcanic and sedimentary strata of the Hazelton Group (uppermost Triassic and Lower to Middle Jurassic), which are cut by the Texas Creek (Early Jurassic) and Cone Mountain (late Early Jurassic) plutonic suites (Fig. 2; e.g., Evenchick et al., 2010; Gagnon et al., 2012; Nelson and Kyba, 2014; Cutts et al., 2015). The Hazelton Group represents

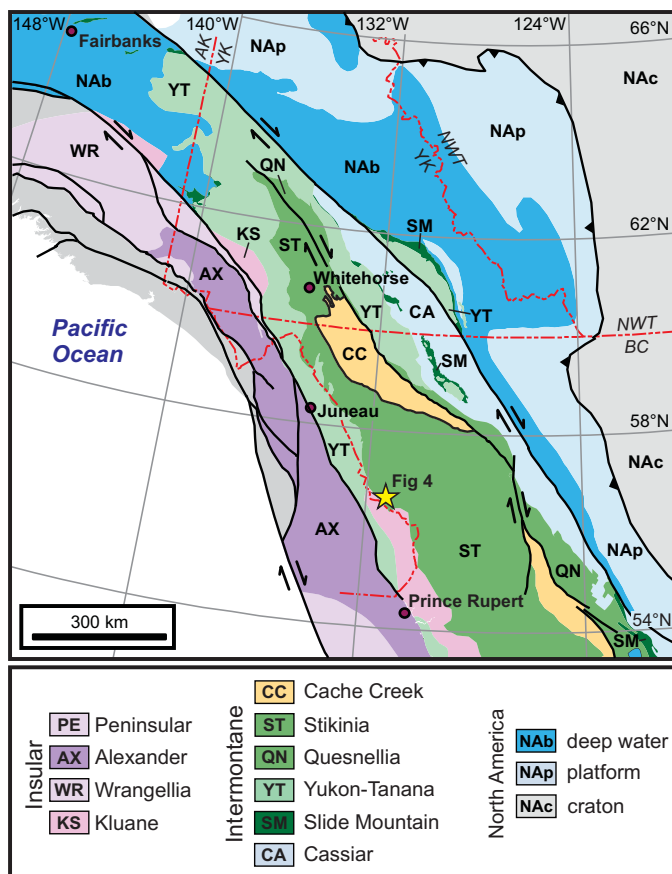


Fig. 1. Geological map of the Canadian Cordillera (from Colpron and Nelson, 2011). Study area (star) is in the Iskut River area of the Stikine terrane.

the final stages of Stikine terrane magmatism before final amalgamation of Stikine, Quesnel, and Cache Creek terranes with North America and deposition of overlap Middle Jurassic to Lower Cretaceous sedimentary rocks of the Bowser Lake Group (Fig. 2; e.g., Evenchick et al., 2007, 2010). Stocks and dikes of the Sloko-Hyder plutonic suite (Eocene) and related volcanic rocks are common in the study area.

The Iskut River area is well known for its prolific mineralization (Fig. 2) including the Eskay, KSM, Brucejack, Snip and Johnny Mountain deposits (Jurassic) and the Burgundy Ridge and Galore Creek deposits (Triassic; e.g., Macdonald et al., 1996). Much of the mineral endowment is spatially associated with hypabyssal porphyritic intrusions (Anderson, 1993) of diverse composition. These plutonic suites include Forrest Kerr and More Creek (Devono-Mississippian), Stikine (Late Triassic), Texas Creek (Early Jurassic), Cone Mountain (late Early Jurassic), Three Sisters (Middle Jurassic) and Sloko-Hyder (Eocene; e.g., Anderson, 1993; Logan and Koyanagi, 1994; Logan et al., 2000; Mihalynuk et al., 2012; Logan and Mihalynuk, 2014). Some members of the Copper Mountain and Texas Creek plutonic suites are distinctive. The Copper Mountain (Late Triassic to Early Jurassic) plutonic suite is conspicuously quartz undersaturated, and includes stocks of foid-bearing syenite, syenite, pyroxenite, gabbro,

and monzodiorite compositions (210-195 Ma; Brown et al., 1996; Zagorevski et al., 2015). The Texas Creek plutonic suite consists of calc-alkaline and alkaline intrusions that vary from granodiorite, to quartz monzonite, and quartz monzodiorite, but includes distinctive crowded plagioclase-phyric diorite, K-feldspar megacrystic monzogranite and syenite (195-189 Ma; Macdonald et al., 1996; Febbo et al., 2015).

3. Surprise Mountain

The Surprise Mountain area is underlain by Triassic to Jurassic epiclastic rocks and marble that are cut by equigranular hornblende quartz diorite (Fig. 4).

3.1. Country rocks

The contact between the epiclastic rocks and marbles is a high-strain zone that includes isoclinal folds in the marble (Fig. 5a) and is interpreted as a thrust fault (Mihalynuk et al., 2012). Along strike to the west are limestones that yielded Permian to Late Triassic conodont fauna (Orchard, 1993). Along the eastern margin of the intrusion, the marble defines a garnet, diopside, actinolite ± wollastonite, quartz, carbonate and pyrite exoskarn (Fig. 5b). Euhedral, zoned garnet has optically isotropic cores and anisotropic rims, typical of skarn garnet that form along the grossular-andradite garnet solid solution series (Deer et al., 1997). Early Jurassic volcanoclastic sedimentary rocks (Mihalynuk et al., 2012) structurally beneath the marble (Fig. 4) consist of buff to green weathering, medium bedded, graded tuffaceous wacke. The tuffaceous component is represented by angular plagioclase fragments and altered mafic minerals.

3.2. Hornblende quartz diorite intrusion

Unfoliated, medium- to coarse-grained equigranular intrusion consists of quartz, plagioclase, K-feldspar, and hornblende (Figs. 6a-c). Although the intrusion is relatively homogeneous, the relative proportion of these minerals varies. Hornblende prisms generally range from <1 mm to 4 mm, but are locally as large as 1 cm (Fig. 6b). Feldspars display carlsbad, polysynthetic, and tartan twinning with discontinuous and oscillatory zoning. Offsets of twin lamellae indicate some deformation of the feldspar grains. Very fine myrmekite is locally present between feldspar and quartz grains. Accessory minerals include magnetite, hematite, pyrite, titanite, apatite, and zircon. Magnetite, abundant in most samples, is partially to extensively replaced by, and/or is intergrown with, high-temperature hematite (Fig. 6d). Locally, zones of magnetite-hematite exsolution are well developed. Pyrite disseminations are common.

The intrusion contains angular to rounded diorite to gabbro enclaves that range from decimetres to a metre in diameter (Fig. 6a). These enclaves may represent cognate xenoliths and/or disaggregated syn-magmatic sills, typical of Cordilleran batholiths (Foster and Hyndman, 1990; Brown et al., 1996). The intrusion is cut by rare mafic dikes, leucocratic dikes that locally form subparallel and conjugate arrays, and a K-feldspar and quartz porphyritic dike. Polymetallic mineralized quartz,

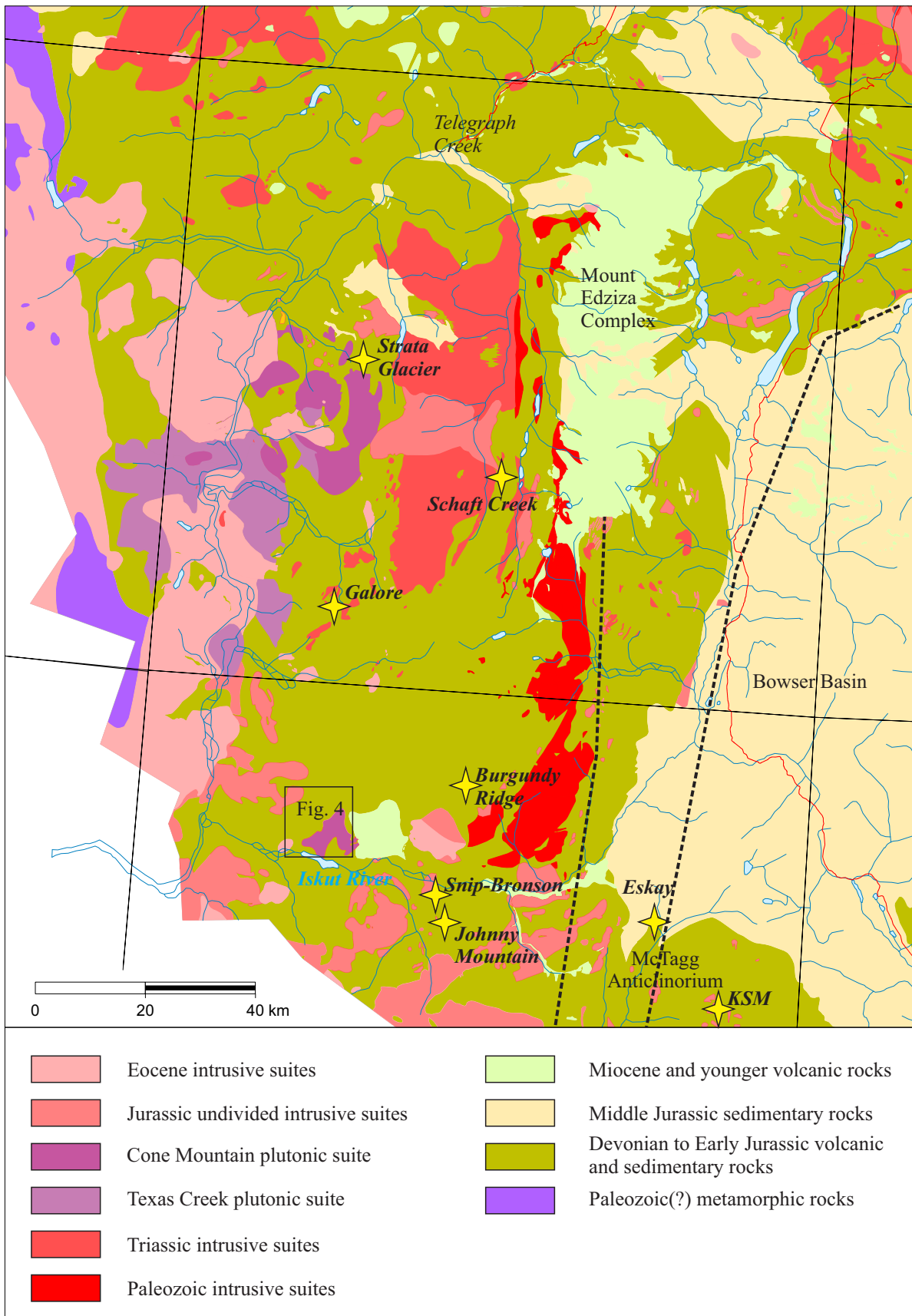


Fig. 2. Simplified geological map of Iskut River – Telegraph Creek area highlighting Mesozoic plutonic suites. Black dashed line is approximate location of the Eskay Rift.

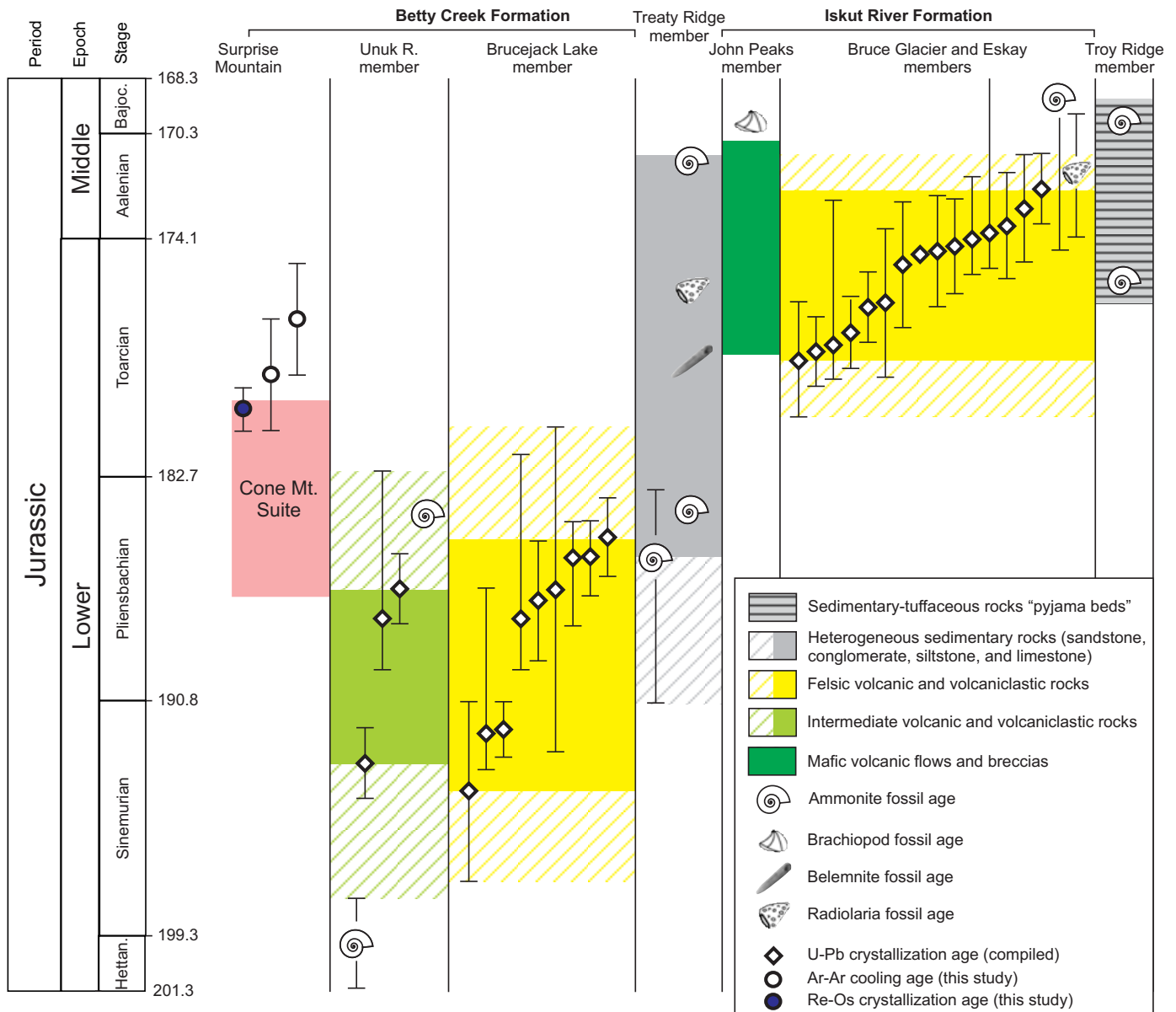


Fig. 3. Summary of Hazelton Group geochronologic and fossil data from the Iskut River area (modified after Cutts et al., 2015) shows a prominent magmatic lull. Data compiled from Macdonald (1993), Childe (1994, 1996), Macdonald et al. (1996), Lewis et al. (2001), Evenchick et al. (2010), Gagnon et al. (2012) and Cutts et al. (2015). Stage boundaries are from Cohen et al. (2013). Age range of the Cone Mountain plutonic suite is from Brown et al. (1996).

and barren epidote and quartz-epidote veins are locally abundant (see below).

3.3. Alteration of the hornblende quartz diorite intrusion

Alteration of quartz diorite is neither pervasive nor intense and generally forms cm- to mm- scale haloes around mineralized quartz veins (Figs. 7a-c). Alteration only partially replaces the primary mineralogy, and consists of sericite, saussurite, epidote, chlorite, carbonate, and Fe-oxide. Alteration intensity varies throughout the intrusion. Some parts contain mainly sericite and saussurite, with minor epidote and no chlorite. Elsewhere, epidote, saussurite, and sericite alteration is predominant, and chlorite is abundant. Alteration of plagioclase to sericite,

saussurite, and epidote is particularly obvious in zoned plagioclase crystals where only cores are altered. Hornblende ranges from pristine to completely replaced by chlorite and minor epidote. Carbonate, Fe-oxide, and clay minerals occur along fractures and in-fill brecciated zones. Pyrite is consistently rimmed by iron hydroxides. Alteration of the quartz diorite is particularly intense near quartz veins as narrow selvages of sericite-saussurite. Overall, the quartz diorite body exhibits a macroscopic bleaching towards the most intensely veined part of the intrusion, probably due to a combination of lower modal hornblende abundance, replacement of hornblende by light-weathering chlorite, and increased sericite and saussurite alteration of feldspar.

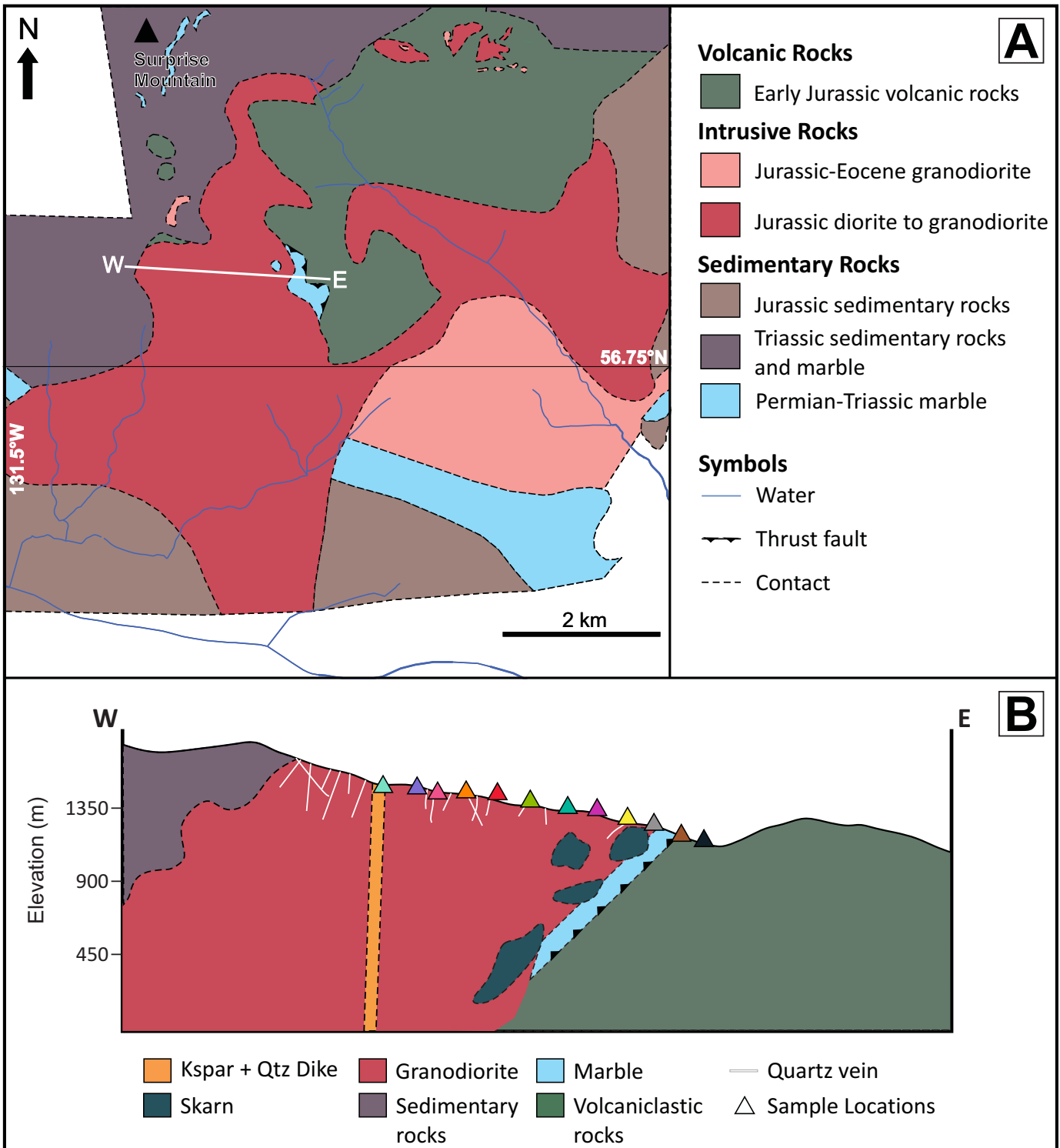


Fig. 4. a) Simplified geological map of the Surprise Mountain area (modified from Mihalyuk et al., 2012). b) Schematic cross-section of quartz diorite and host sedimentary rocks. Approximate sample positions indicated by coloured triangles.

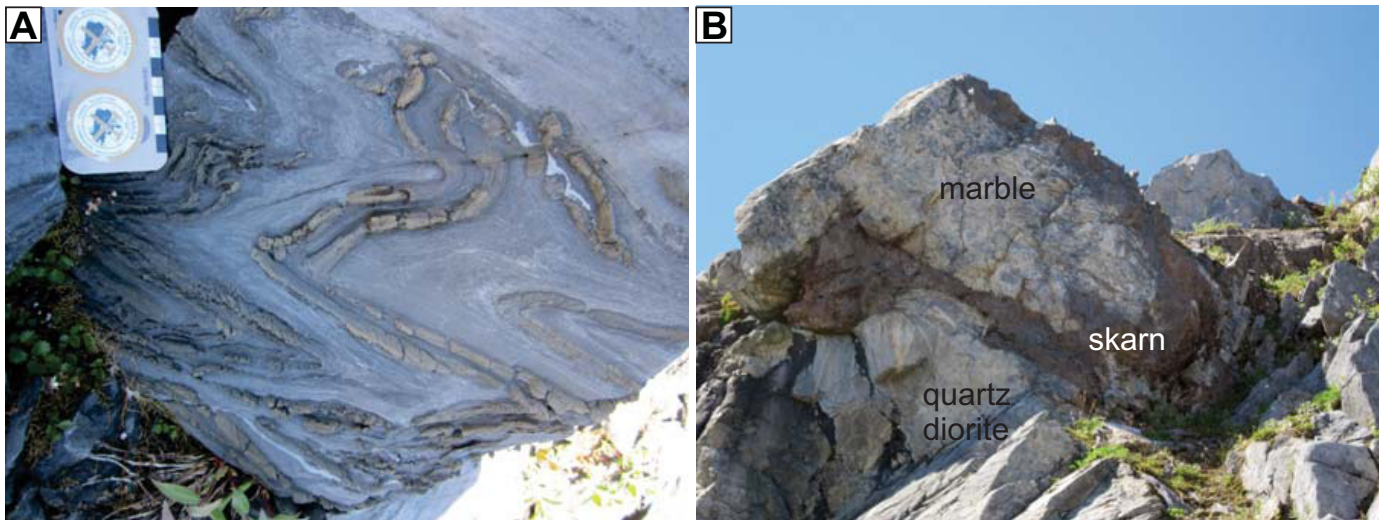


Fig. 5. Permian-Triassic marble, Surprise Mountain area. **a)** Folded (in part isoclinal) layering in immediate hanging wall of thrust fault. Compositional layering in the marble consists of alternating silica and calcite-rich bands. **b)** Marble pod (light toned) in contact with quartz diorite and enveloped by exoskarn.

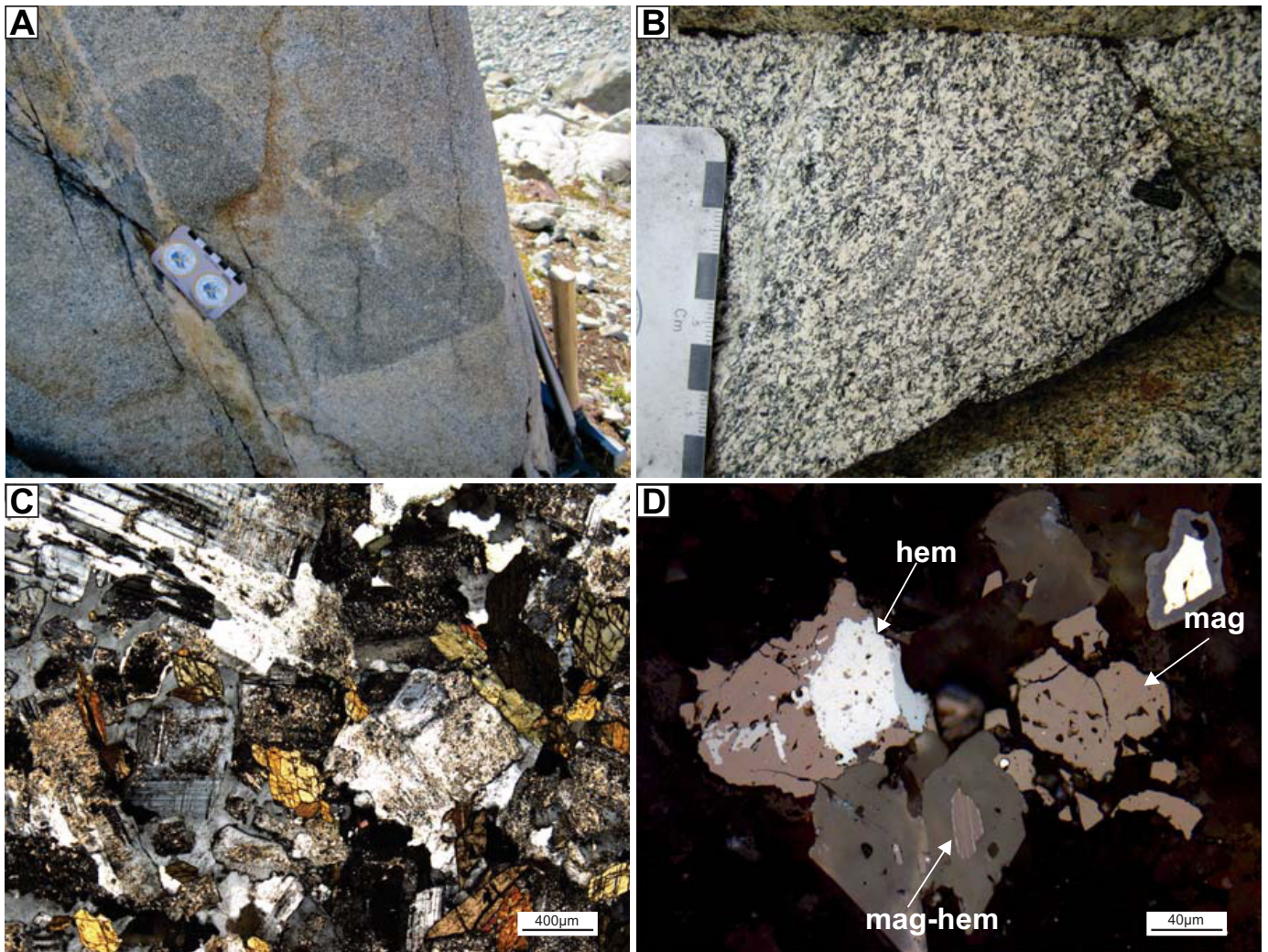


Fig. 6. Hornblende quartz diorite. **a)** Enclaves of diorite in quartz diorite. **b)** Equigranular hornblende quartz diorite (sample ZE573) with sparse hornblende phenocrysts. **c)** Cross-polarized transmitted light view of partially altered quartz diorite. **d)** Polarized reflected light view of magnetite (mag) and hematite (hem), locally exhibiting exsolution texture.

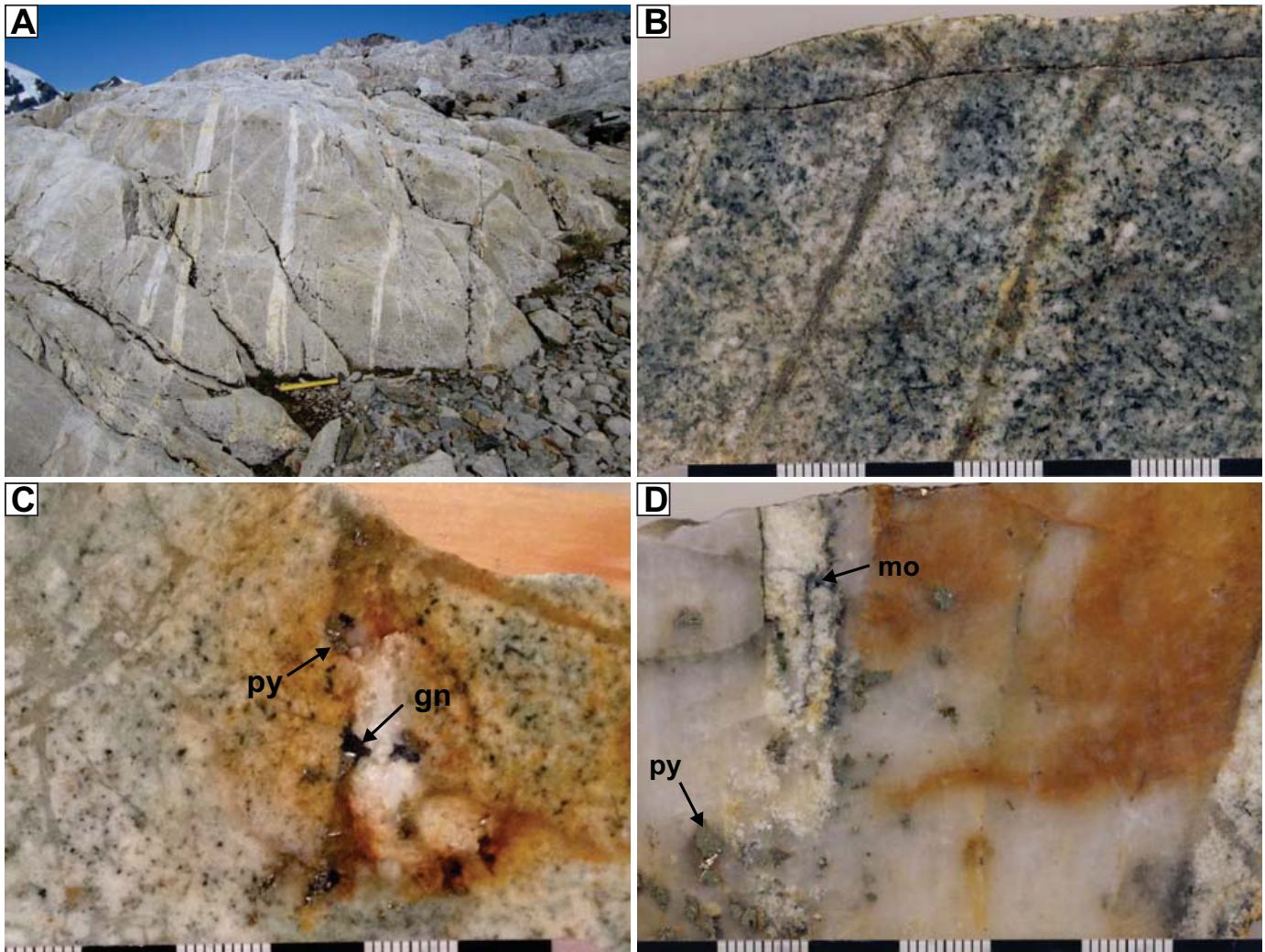


Fig. 7. Quartz veins in quartz diorite intrusion. **a)** Subparallel quartz veins cutting quartz diorite. **b)** Equigranular hornblende quartz diorite cut by thin (4 mm) mineralized quartz veins with narrow alteration haloes (sample K010B). **c)** Bleached granodiorite cut by weakly developed thin quartz vein stockwork, with pyrite (py) and galena (gn) (sample K012A). **d)** Molybdenite (mo) and pyrite (py) mineralization in a 10 cm thick quartz vein (sample K012B).

3.4. Polymetallic veins in the hornblende quartz diorite intrusion

Millimetre- to decimetre- scale quartz veins generally form parallel sets, but also crosscut and form weakly developed stockworks (Figs. 7a, b). The veins trend predominantly ENE-WSW, display moderate to steep dips (~55-70°), and are subparallel to minor ductile shear zones and deformed dikes in the intrusion. Polymetallic sulphides in the quartz veins (Figs. 7c, d) tend to form clots and commonly weather recessively. Mineralized quartz veins tend to be massive and locally fractured and altered by Fe-oxide and hydroxides. Microstructures observable in quartz include deformation lamellae, bulging subgrains and subgrain rotation indicating elevated temperature during deformation (e.g., Passchier and Trouw, 1998).

Mineralization in the quartz veins consists mainly of pyrrhotite, chalcopyrite, and pyrite with subordinate galena, molybdenite, bismuthinite, covellite, chalcocite, magnetite,

ilmenite, and sphalerite. Pyrrhotite, commonly intergrown with chalcopyrite, forms blebs in pyrite (Fig. 8a). Pyrrhotite blebs locally contain sphalerite and bismuthinite. Covellite and chalcocite occur as rims on galena, and inclusions in pyrite (Figs. 8b, c), suggesting replacement of chalcopyrite. Bismuthinite inclusions within pyrite may display zonation from bismuthinite, to native bismuth, with rare zones of Bi-Pb-sulphides (Fig. 8d). Pyrite overprints all minerals except molybdenite and Fe-oxides, which replace pyrite along fractures (Figs. 8e, f). Overprinting of pyrite seems to increase towards the middle of the intrusion where galena, bismuthinite, and molybdenite abundance increases with intensity of pyrite overprint. Replacement of chalcopyrite by covellite and chalcocite, and replacement of pyrite by Fe-oxide and hydroxide is interpreted as late stage alteration.

4. Geochronology

We analyzed hornblende from two quartz diorite samples

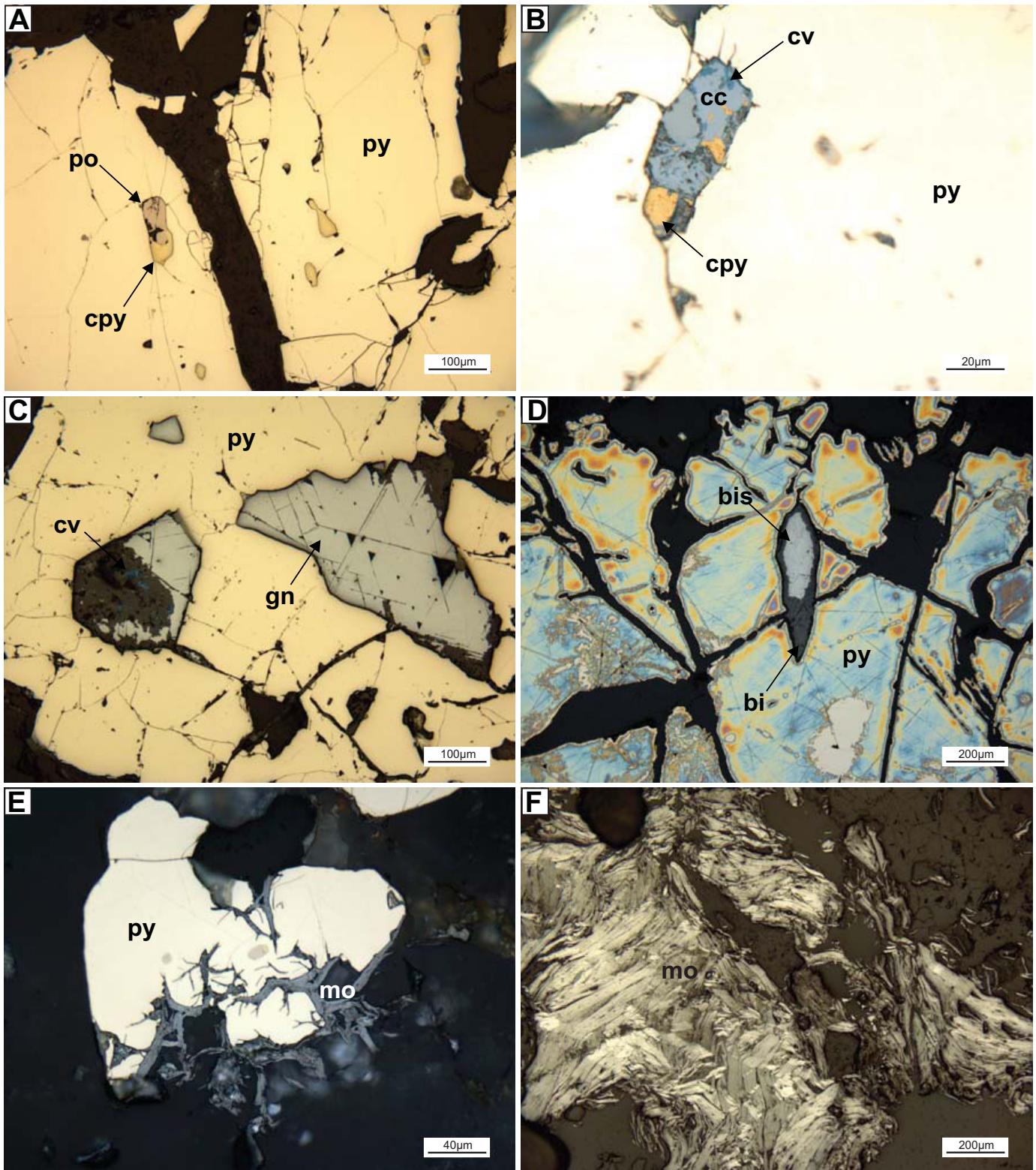


Fig. 8. Mineralization in polymetallic veins. **a**) Polarized reflected light view of chalcopyrite (cpy) and pyrrhotite (po) in pyrite (py). **b**) Polarized reflected light view of covellite (cv) and chalcocite (cc) replacing chalcopyrite (cpy) in pyrite (py). **c**) Polarized reflected light view of pyrite (py) enclosing galena (gn) with late(?) covellite (cv). **d**) Polarized reflected light view of bismuthinite (bis) and bismuth (bi) included in tarnished pyrite (py). **e**) Partly uncrossed polarized reflected light view of molybdenite (mo) replacing pyrite (py) along fractures; pinkish blebs in pyrite are pyrrhotite (po). **f**) Crossed polarized reflected light view of molybdenite (mo) in gangue.

of the Surprise Mountain intrusion using laser $^{40}\text{Ar}/^{39}\text{Ar}$ step-heating and molybdenite from one sample of a crosscutting quartz vein that contains disseminated sulphides using Re-Os isotopes.

4.1. $^{40}\text{Ar}/^{39}\text{Ar}$ methods

Samples 14ZEK009 and 11ZE573 were processed for $^{40}\text{Ar}/^{39}\text{Ar}$ analysis by standard preparation techniques, including hand-picking of fresh unaltered grains of hornblende in the size range 0.25 to 1.0 mm. Individual hornblende separates were loaded into aluminum foil packets along with grains of Fish Canyon Tuff Sanidine (FCT-SAN) to act as flux monitor (apparent age = 28.201 ± 0.023 Ma; 1σ , Kuiper et al., 2008). The sample packets were arranged radially inside two separate aluminum canisters; sample 14ZEK009 was included in sample batch GSC #69 and sample 11ZE573 was included in sample batch GSC #70. Both sample batches were submitted for 160 MWh irradiations (Cd-shielded) in the medium flux position 8B at the research reactor of McMaster University in Hamilton, Ontario, Canada.

Laser $^{40}\text{Ar}/^{39}\text{Ar}$ step-heating analysis was carried out at the Geological Survey of Canada Noble Gas laboratory in Ottawa, Ontario. Upon return from the reactor, samples were split into one or more aliquots each and loaded into individual 1.5 mm-diameter holes in a copper planchet. The planchet was then placed in the extraction line and the system evacuated. Heating of individual sample aliquots in steps of increasing temperature was achieved using a Photon Machines, Inc. Fusions 10.6 55W CO_2 laser equipped with an optical beam-flattening homogenizer lens. The released Ar gas was cleaned in the extraction line over two hot SAESTM NP-10 getters of St 707 alloy (Zr-V-Fe) held at $\sim 400^\circ\text{C}$ (to remove nitrogen, oxygen, hydrocarbons, water and other active gases) and a room-temperature getter containing HY-STOR[®] 201 calcium-nickel alloy pellets (to remove hydrogen), and then analyzed isotopically using a Nu Instruments multicollector Noblesse mass spectrometer, equipped with a Faraday detector and three ion counters. The analyses were run in ion counter multicollection mode ('MC-Y' mode; additional analytical details provided in Kellett and Joyce, 2014). Blank measurements were made throughout the analytical sessions, the values for which are included in the footnotes of Table 1. Mass fractionation and detector efficiencies were determined from repeated measurements of air aliquots carried out throughout the analytical sessions, whereby ^{40}Ar and ^{36}Ar signals were measured on all collectors. $^{40}\text{Ar}/^{36}\text{Ar}$ ratios were then determined for each collector individually, and for each combination of collectors. Detector inter-calibration methods are described in further detail in Kellett and Joyce (2014). Data reduction and age calculations were performed using Mass Spec software version 7.93; details regarding data reduction, error propagation and age calculation are outlined in Deino (2001). The software applies and propagates errors for all corrections, including detector inter-calibration factors.

Corrected argon isotopic data are listed in Table 1, and presented in Figure 9 as spectra of gas release or on inverse-

isochron plots. For gas release spectra, both the apparent ages and plateau ages calculated from the step-heating analyses rely on the assumption that atmospheric argon has a $^{40}\text{Ar}/^{36}\text{Ar}$ ratio of 298.56 (Lee et al., 2006; Mark et al., 2011). For this report, a plateau age is defined as an age derived from three or more consecutive heating steps that are statistically equivalent at 95% confidence level, and comprise greater than 50% of the total ^{39}Ar released. In cases where excess ^{40}Ar is suspected in a sample, data are plotted on the inverse isochron diagram, where $^{36}\text{Ar}/^{40}\text{Ar}$ is plotted against $^{39}\text{Ar}/^{40}\text{Ar}$ for each analysis (after correction for irradiation-produced interfering isotopes and mass spectrometer discrimination; Roddick, 1988).

Neutron flux gradients throughout the sample canister were evaluated by analyzing the FCT-SAN sanidine flux monitors included with each sample packet and interpolating a linear fit against calculated J-factor and sample position. The error on individual J-factor values is conservatively estimated at $\pm 0.6\%$ (2σ). Because the error associated with the J-factor is systematic and not related to individual analyses, correction for this uncertainty is not applied until calculation of dates from isotopic correlation diagrams (Roddick, 1988). Errors in the plateau and inverse isochron ages do not include the errors of decay constants. Nucleogenic interference corrections were $(^{40}\text{Ar}/^{39}\text{Ar})_{\text{K}} = 0.025 \pm 0.005$, $(^{38}\text{Ar}/^{39}\text{Ar})_{\text{K}} = 0.011 \pm 0.010$, $(^{40}\text{Ar}/^{37}\text{Ar})_{\text{Ca}} = 0.002 \pm 0.002$, $(^{39}\text{Ar}/^{37}\text{Ar})_{\text{Ca}} = 0.00068 \pm 0.00004$, $(^{38}\text{Ar}/^{37}\text{Ar})_{\text{Ca}} = 0.00003 \pm 0.00003$, $(^{36}\text{Ar}/^{37}\text{Ar})_{\text{Ca}} = 0.00028 \pm 0.00016$. The decay constant used was $^{40}\text{K}\lambda_{\text{total}} = 5.463 \pm 0.214 \times 10^{-10}/\text{a}$ (2σ) from Min et al. (2000). All errors are quoted at the 2σ level of uncertainty. The 'MSWD' is defined as the mean square of weighted deviates.

4.2. $^{40}\text{Ar}/^{39}\text{Ar}$ results

4.2.1. Sample 14ZEK009; hornblende quartz diorite

Hornblende from this sample is clean, fresh, and dark brown to black. One aliquot was analyzed, yielding a flat four-step plateau, giving an age of 178 ± 2 Ma (Fig. 9a; MSWD = 1.14, 96.8% of total ^{39}Ar). This age overlaps within error with the inverse isochron hornblende age of sample 11ZE573 and Re-Os age (see below).

4.2.2. Sample 11ZE573; equigranular hornblende quartz diorite

Hornblende grains from this sample are clean, fresh, and dark brown. The degassing behaviour of the hornblende was unpredictable and inconsistent from one aliquot to the next, with most of the gas commonly being released in one or two heating steps. Four aliquots were analyzed, each with slightly different heating schedules, with hopes of achieving more evenly-distributed gas releases. An evenly-distributed pattern was not obtained, and three of four aliquots yielded downward-stepping spectra, best exhibited in Aliquot #1 (Fig. 9b, inset 1). Aliquots #2 and #4 gave plateau and pseudo-plateau ages of 183 and 182 Ma, respectively. However, when plotted on the inverse isochron diagram, most data points from all four aliquots fall below the atmospheric line, confirming the

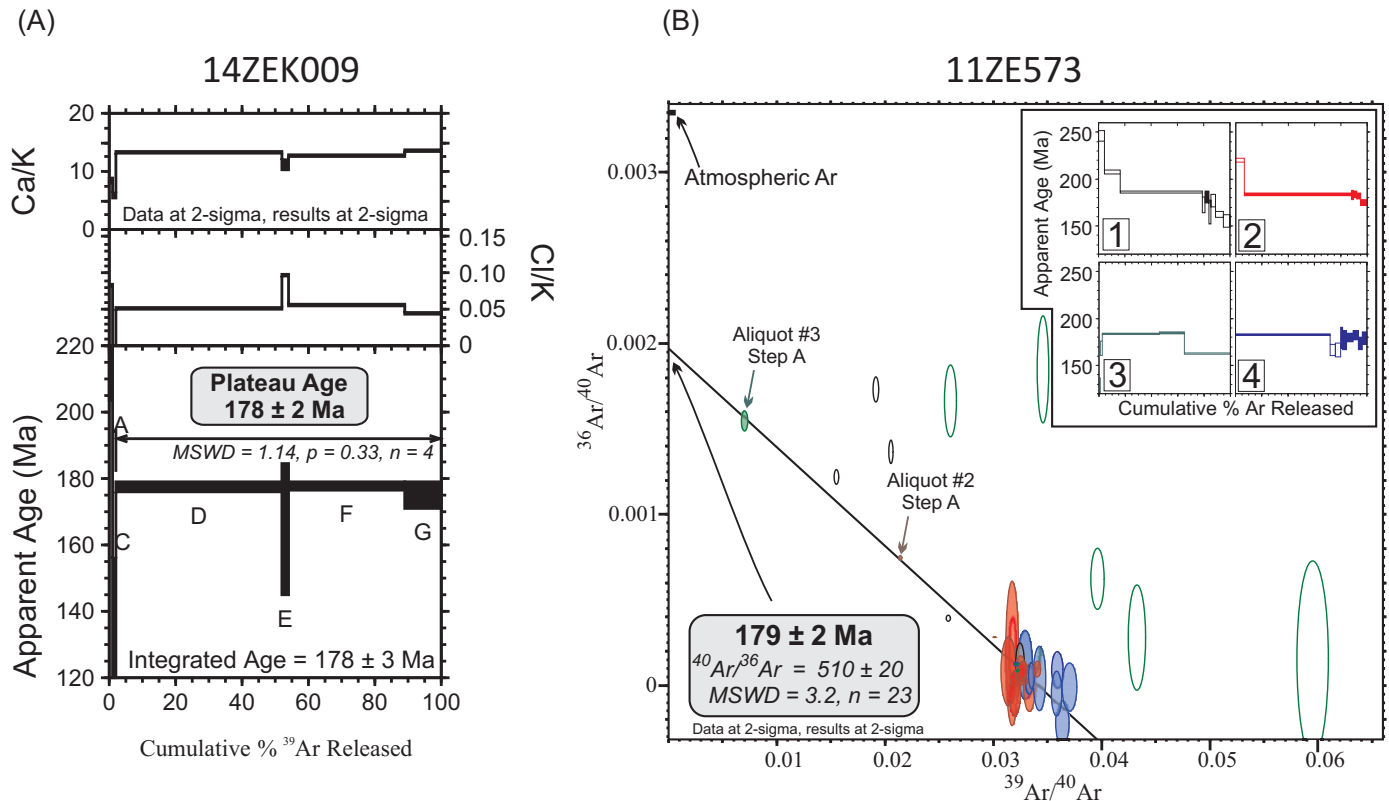


Fig. 9. a) Gas-release spectrum for hornblende from sample 14ZEK009. The integrated age is the total-gas age, calculated by weighting the individual steps by the fraction of ^{39}Ar released. **b)** Inverse isochron plot for hornblende from diorite sample 11ZE573. Colours of ellipses correspond to colours of the aliquots shown in the inset. Filled ellipses are the data points used to calculate the inverse isochron age. Unfilled ellipses were not included in the age calculation. Errors are shown at 2σ . Note that the regression line is heavily controlled by the first heating steps of Aliquots #2 and #3. Inset: Gas-release spectra for Aliquots #1 through #4. The filled boxes are the heating steps that are included in the inverse isochron age calculation. Only the steps comprising greater than 1% of the ^{39}Ar are plotted.

presence of excess ^{40}Ar in the sample (Fig. 9b). The scatter of the 38 data points is likely due to degassing of multiple argon reservoirs of different $^{40}\text{Ar}/^{36}\text{Ar}$ composition, such as mineral and/or fluid inclusions. Heterogeneity within the grains is further evidenced by the variable Ca/K measured throughout the analyses; Ca/K values range between ~ 5 and 22 (Table 1). Using the York (1969) linear least squares regression procedure (invoking the Student's t -test), the inverse isochron age obtained for 23 nearly collinear data points is 179 ± 2 Ma ($\text{MSWD} = 3.2$), corresponding to a trapped Ar composition of $^{40}\text{Ar}/^{36}\text{Ar} = 510 \pm 20$. The regression slope is heavily controlled by only two data points (the first heating steps of Aliquots #2 and #3), whereas the other 21 points are clustered near the x-axis. A more robust inverse isochron age is obtained when the data are spread more evenly along the regression line; however the 179 ± 2 Ma age is considered the best approximation of the hornblende cooling age for this sample.

4.3. Re-Os methods

Re-Os age geochronology of molybdenite was conducted at the University of Alberta, Edmonton, Alberta. A molybdenite mineral separate was made for the sample through metal-free crushing, followed by gravity and magnetic concentration

methods, which are described in detail by Selby and Creaser (2004). The ^{187}Re and ^{187}Os concentrations in the molybdenite separate were determined through isotope dilution mass spectrometry using Carius-tube, solvent extraction, anion chromatography, and negative thermal ionization mass spectrometry techniques. During this process, a mixed double spike containing known amounts of isotopically enriched ^{185}Re , ^{190}Os , and ^{188}Os analysis was used (Markey et al., 2007). Isotopic analysis used a ThermoScientific Triton mass spectrometer by Faraday collector. Total blanks for Re and Os are less than <3 picograms and 2 picograms, respectively, which are insignificant for the Re and Os concentrations in molybdenite. The molybdenite powder HLP-5 (Markey et al., 1998) was analyzed as a standard, and over a period of two years an average Re-Os date of 221.56 ± 0.40 Ma (1SD uncertainty, $n = 10$) was obtained. This Re-Os age date is identical to that reported by Markey et al. (1998) of 221.0 ± 1.0 Ma.

4.3.1. Re-Os results

Sample 14ZEK-012B is from a massive quartz vein containing minor disseminated sulphides that cuts rocks of the Surprise Mountain intrusion. Some quartz grains have deformation lamellae and display undulose extinction. Bands of small

subgrains define minor shear zones in the quartz vein. Pyrrhotite and chalcopyrite occur as inclusions in pyrite. Molybdenite replaces pyrite along fractures and forms aggregates $>400\mu$. The molybdenite mineral separate yielded a Re-Os model age of 180.2 ± 0.8 Ma (Table 2). The age uncertainty is quoted at 2σ (95% confidence) level of precision, and includes all known analytical uncertainty (all sources of error), including the uncertainty in the decay constant of ^{187}Re . Because molybdenite overprints other sulphides, mineralization was before 180.2 ± 0.8 Ma, as was emplacement of the host quartz diorite.

5. Geochemistry of the Surprise Mountain intrusion

Major and trace element geochemical analysis of samples from the Surprise Mountain intrusion (Table 3) followed sample preparation to remove zones of weathering and alteration using a diamond saw. Samples were analyzed by ICP-ES and ICP-MS following lithium metaborate/tetraborate fusion and nitric acid or Aqua Regia digestion at ACME Laboratories (Vancouver, BC; analytical packages 4A4B and 1DX) and Activation Laboratories (Ancaster, ON; analytical package 4Lithores). The accuracy is typically 5 to 20% if the analyte is at least 10 times the stated detection limit.

Calculated modal mineral contents indicate that the composition of the intrusion varies broadly from granodiorite, quartz diorite to quartz monzodiorite (Fig. 8a; Whalen and Frost, 2013), consistent with modal mineral variations observed in samples. All samples plot along the calc-alkalic magmatic trend (Fig. 10a). Calculated $\text{Fe}_2\text{O}_3/\text{FeO}$ ratios (Irvine and Baragar, 1971) for all samples exceed 0.5, indicative of magnetite-series granitic rocks (Ishihara 1977, 1981). This is consistent with the common presence of magnetite and high-temperature hematite, and relatively high magnetic susceptibility (average 15.8×10^{-3} SI).

On normalized extended trace element plots (Fig. 10) samples yield similar trace element profiles. Samples normalized to primitive mantle (Fig. 10b) show an overall enrichment of large ion lithophile elements (LILE), and an enrichment of light rare earth elements (LREE) relative to heavy rare earth elements (HREE). The samples also display depletion of high field strength elements Nb, Ta, and Ti. Samples normalized to petrographically least altered sample K004, yield very similar trace element profiles, indicating only small differences between samples (Fig. 10c). The largest differences are in Cs, Rb Nb, K and Pb. The homogeneity in major and trace element contents displayed by samples from the Surprise Mountain intrusion suggests limited assimilation, fractionation, and alteration.

6. Geochemistry of mineralization

We analyzed 12 mineralized samples from the Surprise Mountain intrusion (Table 4). Samples were cut using a diamond saw to retain representative slabs of mineralized zones for petrographic analysis and a split was submitted for geochemistry. Major and trace elements were analyzed using ICP-ES and ICP-MS following lithium metaborate/tetraborate

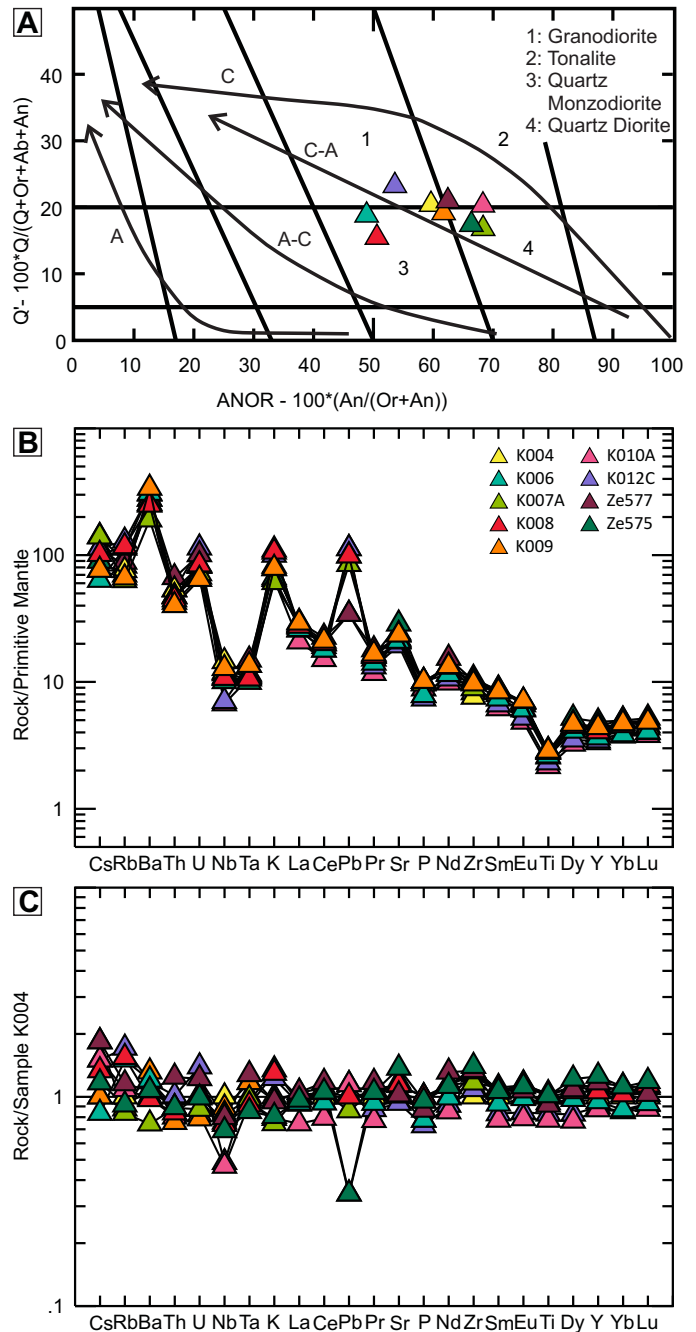


Fig. 10. Geochemical characteristics of quartz diorite. **a)** Normative quartz-feldspar discrimination diagram (Whalen and Frost, 2013). **b)** Primitive mantle-normalized extended trace element plot (values from Sun and McDonough, 1989). **c)** K004-normalized extended trace element plot.

fusion and Aqua Regia digestion at ACME Laboratories (Vancouver, BC; analytical package 1DX) and Activation Laboratories (Ancaster, ON; analytical package AQ251_EXT). Accuracy is typically in the 1-3% range as long as the analyte is present at 20 times the detection limit.

Analytical results show wide variability of all elements, with the exception of Ag, which is consistently elevated in all samples

Table 2. Re-Os isotopic data and ages.

Sample	Re ppm	$\pm 2\sigma$	^{187}Re ppb	$\pm 2\sigma$	^{187}Os ppb	$\pm 2\sigma$	Model Age (Ma)	$\pm 2\sigma$ (Ma)
142EK-012B	55.55	0.16	34.92	0.1	105	0.1	180.2	0.8

relative to the host intrusion, in which Ag is consistently below the detection limit (<0.5 ppm). Some samples are elevated in Bi, Pb, Mo, and W relative to host intrusion where these elements are below or at the detection limit (0.1, 5, 2, 0.5 ppm respectively). Au is consistently near the limits of detection in all samples.

7. Discussion

7.1. Relationship between the Surprise Mountain intrusion and the Cone Mountain plutonic suite and timing of thrusting, intrusion, and mineralization

The $^{40}\text{Ar}/^{39}\text{Ar}$ (178 ± 2 and 179 ± 2 Ma) cooling and Re-Os mineralization (180.2 ± 0.8 Ma) ages and the lithological characteristics described above suggest that the Surprise Mountain pluton is part of the Cone Mountain plutonic suite (187-180 Ma), and part of a north-trending belt from the Iskut River to Telegraph Creek (Fig. 2). Brown et al. (1996) noted that the Cone Mountain suite characteristically contains abundant angular diorite enclaves, as is seen in the Surprise Mountain quartz diorite, and a common feature in calc-alkaline granitic rocks (Foster and Hyndman, 1990).

Quartz diorite cuts isoclinally folded Triassic marble and cuts across the thrust contact between this marble and structurally underlying volcano-sedimentary rocks (Fig. 4). Thus thrusting must have been before ~ 180 Ma (age of the late syn-intrusive mineralization) and after deposition of the footwall volcano-sedimentary rocks that are intercalated with ~ 187 Ma dacitic tuff breccia to the northeast (Zagorevski et al. unpublished data). This is similar to the relationship observed to the north, where Pliensbachian volcanic rocks ($185 \pm 7/-2$ Ma; Brown et al., 1996) unconformably overlie folds and thrusts developed in the Stuhini Group. Emplacement of the quartz diorite broadly coincides with the volcanic lull at the transition from the subaerial and marine arc-related Betty Creek formation to rift related submarine magmatism of the Iskut River Formation in the Eskay rift (Fig. 2; Gagnon et al., 2012; Lewis et al., 2013). These stratigraphic relationships are well displayed on the flanks of the McTagg anticlinorium to the east (Fig. 2; Cutts et al., 2015 and references therein). This fundamental tectonic shift was accompanied by a change from porphyry-epithermal styles to volcanogenic massive sulphide styles of mineralization (e.g., Macdonald et al., 1996).

7.2. Polymetallic vein mineralization

Sheeted, subparallel mineralized quartz veins (Fig. 11) suggest emplacement in a dilatational brittle regime. Textural relationships between mineral phases suggest three

mineralizing events: 1) early polymetallic mineralization, with mainly pyrite; 2) an overprinting molybdenum-rich event; and 3) a late, more oxidized event leading to Cu remobilization and deposition of chalcocite and covellite. It is unclear if the different compositions recorded by these events resulted from continuous fluid evolution or from distinct fluid pulses overprinting earlier assemblages.

Despite the apparent lack of Au in the polymetallic veins (≤ 15 ppb), the occurrence displays high concentrations of Au indicator elements including Bi (>2000 ppm) and W (>100 ppm) (Robb, 2005). Strong enrichment of Ag (up to 17 ppm) may be correlated with Au elsewhere within the system (e.g., Robb, 2005). Lack of elevated Au in all 12 samples analyzed suggests that the analyzed Au contents are representative of the sheeted veins in this area. The principal hydrothermal fluids appear to have been lacking Au in this part of the system.

The nature of the mineralization, including association with vein arrays, sulphide mineral assemblage, Ag enrichment, and lack of alteration are most consistent with polymetallic Ag-Pb-Zn \pm Au or Cu \pm Ag quartz deposit types (Lefebure and Church, 1996). These deposits typically display limited alteration and an association with calc-alkaline granitic rocks and are contained by steeply dipping, narrow, tabular or splayed subparallel vein sets. These deposits may be peripheral to skarn or porphyry mineralization (Lefebure and Church, 1996) as is observed at Surprise Mountain, where mineralization is close to a garnet, diopside, actinolite \pm wollastonite, quartz, carbonate and pyrite exoskarn. The true nature and full regional extent of the alteration and mineralization remains unclear, as pathfinder metals such as Bi and W were not traced outside of the study area, and skarn was not investigated for potential mineralization. However, quartz-carbonate veins with disseminated galena, sphalerite, tetrahedrite, and arsenopyrite were previously reported on the northeastern margin on this intrusion (MINFILE 104B 130). These yielded assays of up to 1698 grams per tonne silver and up to 12.75 grams per tonne gold (Holbek, 1983).

7.3. Comparison to other Jurassic deposits in the Iskut River area

Significant deposits near the Surprise Mountain body include Red Bluff, Snip, and Johnny Mountain, all of which are older (Fig. 2). The Red Bluff intrusion (195 ± 1 Ma; Macdonald et al., 1996) consists of K-feldspar megacrystic, plagioclase porphyritic quartz diorite to quartz monzonite (Burgoyne and Giroux, 2007). In contrast to the Surprise Mountain body, the Red Bluff intrusion is moderately to intensely hydrothermally altered by K-feldspar-biotite-magnetite and later sericite-

Table 3. Whole rock geochemical data.

Sample	DL*	K003C	K004	K006	K007A	K008	K009	K010A	K012C	ZB567*	ZES75*	ZB577*
UTM Easting		351337	351317	351051	350981	350856	350856	350359	349995	352793	351057	350463
UTM Northing		6293238	6293220	6293225	6293237	6293344	6293344	6293434	6293655	6292634	6293284	6293413
Rock Type		Monzogranite Dike	Granodiorite-Monzodiorite	Quartz Monzodiorite	Quartz Diorite	Quartz Monzodiorite	Quartz Monzodiorite	Diorite-Tonalite	Granodiorite	Quartz Gabbro Dike	Quartz Diorite	Granodiorite-Tonalite
SiO ₂	0.01%	72.64	62.27	63.5	59.68	61.41	62.34	63.17	64.18	60.59	61.23	62.84
Al ₂ O ₃	0.01%	13.43	16.24	16.44	16.98	16.84	16.72	17.48	16.05	17.36	16.9	16.56
Fe ₂ O ₃	0.01/0.04%	1.15	5.34	4.96	5.65	3.81	5.76	4.47	5.83	4.37	5.31	5.31
MnO	0.001/0.01%	0.035	0.117	0.117	0.143	0.087	0.144	0.122	0.122	0.11	0.13	1.75
MgO	0.01%	0.32	1.79	1.53	1.91	1.68	1.96	1.29	1.53	2.05	1.79	0.14
CaO	0.01%	2.01	5.64	4.64	5.56	5.91	5.73	5.86	4.84	6.91	6.17	5.61
Na ₂ O	0.01%	2.7	3.47	3.65	3.92	3.84	3.57	3.85	3.2	4.41	3.84	3.44
K ₂ O	0.01%	5.48	2.46	3.31	1.83	3.19	2.37	1.94	3.01	0.39	1.98	2.33
TiO ₂	0.001/0.01%	0.178	0.603	0.565	0.625	0.603	0.617	0.466	0.499	0.67	0.61	0.55
P ₂ O ₅	0.01%	0.03	0.22	0.17	0.21	0.22	0.22	0.17	0.16	0.23	0.21	0.19
LOI	0.01/0.1%	0.79	0.98	0.95	2.9	0.88	1.49	1.7	1.24	1.7	0.9	1
Total	%	98.78	99.17	99.84	99.41	98.48	100.9	99.65	99.21	99.8	99.65	99.66
Ba	3/5ppm	1979	1789	2150	1327	1735	2354	1765	2114	526	1917	1911
Be	1ppm	<1	1	1	1	1	1	1	1	1	<1	1
Ce	0.05/0.1ppm	14.2	33.8	31.6	35.4	35.7	37.2	26.7	31.7	36.1	35.6	39.6
Cr	20ppm	80	30	20	30	30	20	40	30	N/A	N/A	N/A
Cs	0.1ppm	0.9	0.6	0.5	1.1	0.8	0.6	0.9	0.9	0.1	0.7	1.1
Dy	0.01/0.05ppm	0.96	3.11	3.02	3.46	3.29	3.42	2.38	2.57	3.87	3.78	3.36
Er	0.01/0.03ppm	0.65	1.93	1.91	2.27	2.04	2.22	1.57	1.58	2.27	2.22	2.08
Eu	0.005/0.02ppm	0.224	1.03	1.01	1.17	1.18	1.19	0.81	0.87	1.18	1.15	1.1
Ga	1/0.5ppm	13	18	17	18	17	18	19	17	16.6	18.9	17.6
Gd	0.01/0.05ppm	0.91	3.1	2.98	3.63	3.42	3.26	2.55	2.54	3.53	3.66	3.54
Ge	0.5ppm	1.4	1.2	1.3	1.4	1.2	1.2	1.5	2	N/A	N/A	N/A
Hf	0.1ppm	1.8	2.4	2.4	2.7	2.2	2.9	2.7	2.3	3.5	3.4	3.4
Ho	0.01/0.02ppm	0.2	0.67	0.61	0.73	0.67	0.69	0.5	0.52	0.75	0.76	0.73
La	0.05/0.1ppm	15.7	19.1	17.8	19.5	18.9	20	14.2	17.6	17.6	18.4	20.1
Lu	0.002/0.01ppm	0.126	0.321	0.298	0.362	0.365	0.356	0.28	0.295	0.36	0.38	0.33
Nb	0.2/0.1ppm	1.2	10.3	7.8	8.5	7.6	9.1	4.8	5	7.3	7.1	8.2
Nd	0.05/0.3ppm	5.36	15.7	15.5	18	17.7	17.9	13.3	14.3	17.4	17.6	20.6
Pr	0.01/0.02ppm	1.62	4.18	3.89	4.5	4.39	4.58	3.22	3.63	4.55	4.39	4.9
Rb	1/0.1ppm	119	48	72	40	74	42	52	82	5.8	43.9	55.4
Sm	0.01/0.05ppm	0.93	3.53	3.26	3.91	3.75	3.71	2.73	2.93	3.92	3.74	3.83
Sr	2/0.5ppm	230	437	441	460	499	495	513	407	519.3	598.7	446.2
Ta	0.01/0.1ppm	0.18	0.47	0.45	0.46	0.43	0.55	0.44	0.55	0.6	0.4	0.6
Tb	0.01ppm	0.15	0.49	0.49	0.56	0.53	0.54	0.42	0.42	0.6	0.61	0.55
Th	0.05/0.2ppm	8.83	4.51	3.99	3.99	3.78	3.4	3.61	4.56	4.4	4	5.6
Tm	0.005/0.01ppm	0.103	0.312	0.294	0.352	0.328	0.334	0.26	0.263	0.37	0.34	0.32
U	0.01/0.1ppm	2.96	1.72	1.74	1.5	1.76	1.35	1.41	2.39	1.7	1.7	2.1
V	5/8ppm	23	119	96	117	103	118	85	103	112	127	96
Y	0.5/0.1ppm	7.1	17.4	16.5	18.8	18.4	19.9	15.1	15.6	22	21.8	20.3
Yb	0.01/0.05ppm	0.75	2.18	1.89	2.41	2.23	2.31	1.86	1.85	2.21	2.43	2.45
Zr	1/0.1ppm	61	85	110	99	112	108	113	92	122	118.7	113.4

UTM Zone 9, NAD 83

□ Samples analyzed at Activation Laboratories Ltd., Ancaster, Ontario, 2014

*Samples analyzed at Acme Analytical Laboratories Ltd., Vancouver, British Columbia, 2011

Table 4. Assay data.

Sample	DL □ *	K002A □	K003B □	K010B □	K011A □	K011B □	K011C □	K012A3 □	K012A2 □	K012A4 □	K012B □	ZE578A *	ZE578B *
UTM Easting		0351610	0351337	0350359	0350067	0350067	0350067	0349995	0349995	0349995	0349995	0350004	0350004
UTM Northing		6292989	6293238	6293434	6293613	6293613	6293613	6293655	6293655	6293655	6293655	6293637	6293637
Rock Type		Quartz Vein	Quartz Vein	Host & Quartz Vein	Host & Quartz Vein	Quartz Vein	Host & Weak Quartz Vein	Quartz Vein					
		Stockwork											
Ag	100/2ppb	309	387	82	255	74	17549	1331	210	7251	219	2900	300
As	0.5/0.1ppm	<0.1	2.7	0.4	0.8	0.3	0.7	1.2	0.6	<0.1	<0.1	<0.5	<0.5
Au	10/0.2ppb	2.4	3.3	1.3	4.6	0.9	14.8	3	3.7	2.9	2.4	5.5	0.6
Bi	0.1/0.02ppm	0.21	0.11	0.16	0.98	3.9	174.24	2.89	8.63	14.41	1.3	>2000.0	766.6
Cd	0.1/0.01ppm	0.05	0.61	0.06	0.12	<0.01	0.03	0.06	<0.01	0.52	0.47	<0.1	<0.1
Co	0.1ppm	22.1	13.9	8	3.3	0.7	1.4	1.8	0.2	4.2	2.6	2	0.6
Cu	0.1/0.01ppm	210.54	92.46	61.53	66.6	12	36.63	42.37	25.64	55.64	23	28.3	9.7
Fe	0.01%	3.36	2.19	2.15	1.81	1.05	3.31	3.25	1.21	1.69	1.67	2.01	0.89
Mn	1ppm	158	110	397	345	38	59	152	32	192	45	12	11
Mo	0.1/0.01ppm	0.62	6.72	10	0.85	182.24	113.92	67.21	15.33	9.2	764.94	46.2	8
Ni	0.1/0.1ppm	15.5	21.9	1.9	1.4	0.7	0.9	0.9	0.7	1.4	1	3.4	3.8
Pb	0.1/0.01ppm	2.64	40.02	4.15	3.64	3.25	22.84	443.44	5.54	2799.85	6.98	46	22.6
Re	1ppb	<1	16	<1	<1	3	2	<1	<1	<1	62	N/A	N/A
Sb	0.1/0.02ppm	0.11	0.47	0.07	0.02	0.03	0.15	0.58	0.06	0.1	0.08	1.5	0.5
Se	0.5/0.1ppm	6.7	4	0.4	0.6	0.8	8.5	1.8	1.4	2.3	1.8	10.1	4.6
Sn	0.1ppm	<0.1	0.3	0.2	<0.1	<0.1	<0.1	0.6	<0.1	0.3	<0.1	N/A	N/A
Te	0.2/0.02ppm	0.22	0.12	0.03	0.05	0.2	1.93	0.18	0.14	0.27	0.05	3.9	1.5
W	0.1ppm	2	0.3	0.7	53.7	7.5	3.6	0.8	3.1	0.3	>100	41.3	>100.0
Zn	1/0.1ppm	23.6	145	38.1	26.9	7	8.5	20.5	5.6	24.2	5.2	4	2

UTM Zone 9, NAD 83

□ Samples analyzed at Activation Laboratories Ltd., Ancaster, Ontario, 2014

* Samples analyzed at Acme Analytical Laboratories Ltd., Vancouver, British Columbia, 2011

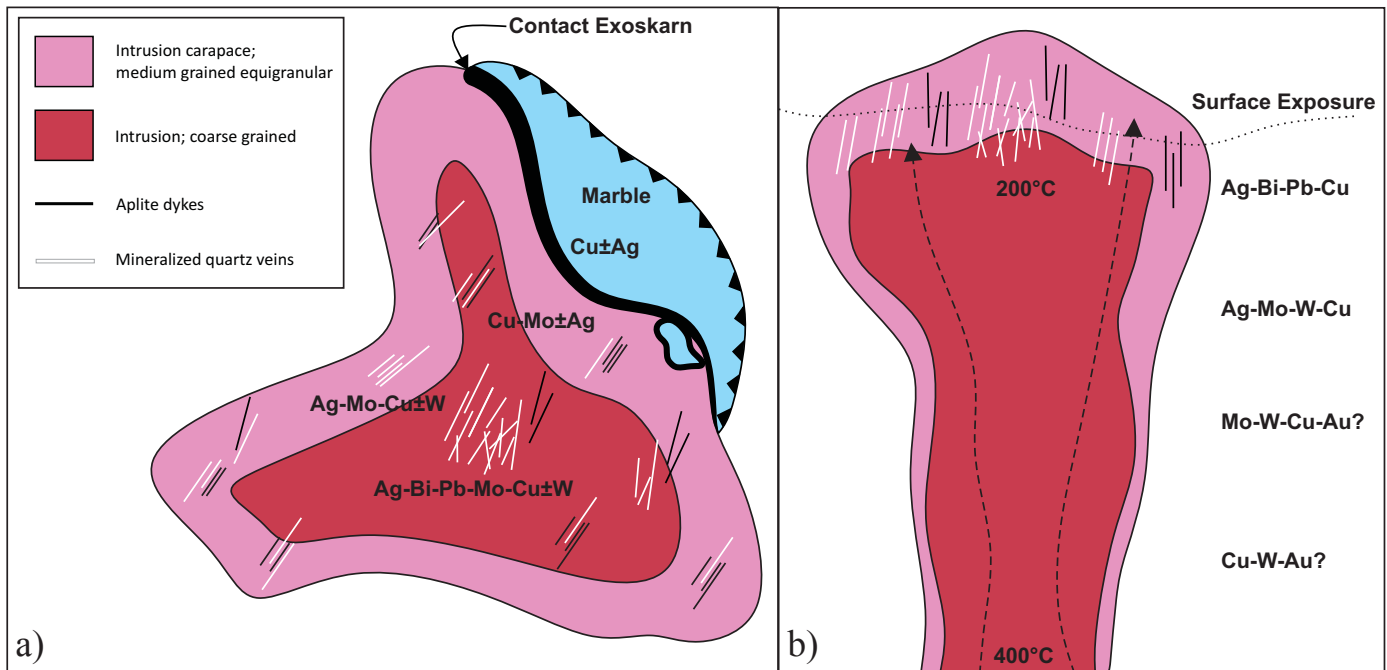


Fig. 11. Schematic model for polymetallic vein mineralization near Surprise Mountain in plan view **a)** and vertical cross-section **b)**. Present erosion level may expose only the shallow, low-temperature part of the mineralizing system.

quartz-pyrite-albite assemblages (Macdonald et al., 1996; Burgoyne and Giroux, 2007). Mineralization comprises quartz-magnetite-hematite stockwork veins, disseminated pyrite-chalcocopyrite, quartz-Fe-oxide stockwork, and quartz-pyrite-chalcocopyrite veins and veinlets (Burgoyne and Giroux, 2007). The related Snip (Au-Cu-Mo) and Johnny Mountain (Au-Ag-Pb-Zn) deposits are precious metal-rich veins hosted by Triassic and Jurassic sedimentary rocks, and are spatially and genetically related to the Red Bluff porphyry deposit (Burgoyne and Giroux, 2007). At Snip, syn-tectonic quartz and sulphide veins (pyrite-pyrrhotite) were emplaced in a southwest-dipping brittle-ductile fault zone (Macdonald et al., 1996). At Johnny Mountain, auriferous quartz-pyrite veins commonly contain pyrrhotite, chalcocopyrite, sphalerite, magnetite, pyrrhotite, and galena (Macdonald et al., 1996). Veins are typically 0.5 to 2 m thick and are surrounded by potassium feldspar alteration envelopes that are up to several times the vein width (Macdonald et al., 1996). The intensity and character of alteration and the potassic character of the host intrusion distinguishes the Red Bluff, Snip, and Johnny Mountain deposits from the Surprise Mountain occurrence, where the alteration is limited to narrow haloes around veins, and the host pluton is a calc-alkalic quartz diorite. Calc-alkalic members of the Cone Mountain plutonic suite at the Strata Glacier pluton (Fig. 2) are associated with polymetallic vein systems (Brown et al., 1996) suggesting that these may be more prospective than previously known.

8. Conclusions

The Surprise Mountain intrusion is a calc-alkaline, I-type, magnetite-series, medium- to coarse-grained, equigranular hornblende quartz diorite. The intrusion cuts a northeast-

vergent thrust fault that stacked Permian to Late Triassic marbles above Early Jurassic (<187 Ma) volcanoclastic rocks. Samples from the intrusion yielded $^{40}\text{Ar}/^{39}\text{Ar}$ hornblende cooling ages of 178 ± 2 and 179 ± 2 Ma. An Upper-Lower Jurassic molybdenite Re-Os age of 180.2 ± 0.8 Ma defines the minimum age of mineralization, and the minimum age of the host intrusion, implying that thrusting was between ~187 and 180 Ma. Lithological variation and enclave abundance, in conjunction with the minimum 180.2 ± 0.8 Ma age, suggest that the intrusion is part of the Cone Mountain plutonic suite (187-180 Ma). Polymetallic mineralization displays high concentrations of indicator elements including Bi (>2000 ppm) and W (>100 ppm), consistent enrichment of Ag (≤ 17 ppm), significant Pb (>2000 ppm) and Mo (>700 ppm), and trace amounts of Au (≤ 14.8 ppb). Low Au contents, weak alteration, and lack of metal zonation differentiates this occurrence from nearby porphyry-related vein deposits like Snip and Johnny Mountain, 20 km to the east-southeast. Sheeted quartz veins in the Surprise Mountain quartz diorite are part of a weakly-developed intrusion-hosted polymetallic vein system. This system displays an Ag-Bi-Pb-Mo-Cu elemental association that is not well known in the Iskut River area. Despite the lack of analyzed Au, persistently elevated Ag and other pathfinder elements, especially W and Bi, suggest that the sheeted vein system warrants further investigation. Additionally, strong skarn development in marble in the hanging wall of a thrust fault should be evaluated, especially considering that Au-bearing skarns are documented around other Cone Mountain plutonic suite intrusive rocks (Brown et al., 1996). Further work is necessary to determine the spatial extent of mineralization in the Surprise Mountain intrusion, and to better determine the

relationship between Cone Mountain plutonic suite bodies and polymetallic vein mineralization in northwestern British Columbia.

Acknowledgments

This research forms part of K. Martin's B.Sc. thesis at the University of Ottawa, Ottawa that was supported by GEM2: Cordillera Project. J. Nelson and J. Kyba are gratefully acknowledged for providing logistical support for this project. J. Nelson and L. Aspler are thanked for their thoughtful suggestions which improved this manuscript.

References cited

- Anderson, R.G., 1993. A Mesozoic stratigraphic and plutonic framework for northwestern Stikinia (Iskut River area), northwestern British Columbia, Canada. In Dunne, G. C., and McDougall, K. A., (Eds.), *Mesozoic paleogeography of the western United States - II: Los Angeles*. Society of Economic Paleontologists and Mineralogists, Pacific Section, Book 71, p. 477-494.
- Anderson, R.G., and Thorkelson, D.J., 1990. Mesozoic stratigraphy and setting for some mineral deposits in Iskut River map area, northwestern British Columbia. Geological Survey of Canada, Paper 90-1E, 131-139.
- Brown, D.A., Gunning, M.H., and Greig, C.J., 1996. The Stikine project: geology of western Telegraph Creek map area, northwestern British Columbia (NTS104G/5, 6, 11W 12 and 13). British Columbia Ministry of Energy, Mines and Petroleum Resources, British Columbia Geological Survey Bulletin 95, 183p.
- Burgoyne, A.A. and Giroux, G.H., 2007. Technical Report on the Bronson Slope Property, Northwestern British Columbia, Canada. Skyline Gold Corporation, Vancouver, BC. 145 p. (downloaded from <http://www.snipgoldcorp.com/s/BronsonSlope.asp> on April 27, 2015).
- Childe, F.C., 1994. Radiogenic isotopic investigations of the Eskay Creek volcanic hosted massive sulphide deposit, British Columbia, Canada. United States Geological Survey Circular 1107, 58p.
- Childe, F.C., 1996. U-Pb geochronology and Nd and Pb isotope characteristics of the Au-Ag-rich Eskay Creek volcanogenic massive sulfide deposit, British Columbia. *Economic Geology*, 91, 1209-1224.
- Cohen, K.M., Finney, S.C., Gibbard, P.L. and Fan, J.-X., 2013. The ICS International Chronostratigraphic Chart. *Episodes* 36, 199-204.
- Colpron, M., and Nelson, J.L., 2011. A Digital Atlas of Terranes for the Northern Cordillera. British Columbia Ministry of Energy and Mines, British Columbia Geological Survey GeoFile 2011-11.
- Cutts, J.A., McNicoll, V.J., Zagorevski, A., Anderson, R.G., and Martin, K., 2015. U-Pb geochronology of the Hazelton Group in the McTagg anticlinorium, Iskut River area, northwestern British Columbia. In: *Geological Fieldwork 2014*, British Columbia Ministry of Energy and Mines, British Columbia Geological Survey Paper 2015-1, pp. 87-101.
- Deer, W.A., Howie R.A., and Zussman, J., 1997. *Rock Forming Minerals*, Volume 1A: Orthosilicates, Geological Society, London, 919p.
- Deino, A.L., 2001. Users' manual for Mass Spec v. 5.02. Berkeley Geochronology Center Special Publication 1a, 119p.
- Evenchick, C.A., Poulton, T.P., and McNicoll, V.J., 2010. Nature and significance of the diachronous contact between the Hazelton and Bowser Lake Groups (Jurassic), north-central British Columbia. *Bulletin of Canadian Petroleum Geology*, 58, 235-267.
- Evenchick, C.A., Sears, J.W., McMechan, M.E., McNicoll, V.J., Carr, S.D., Harms, T.A., and Evenchick, C.A., 2007. A synthesis of the Jurassic-Cretaceous tectonic evolution of the central and southeastern Canadian Cordillera; exploring links across the orogen. *Geological Society of America, Special Paper*, 433, 117-145.
- Febbo, G.E., Kennedy, L.A., Savell, M., Creaser, R.A., and Friedman, R.M., 2015. Geology of the Mitchell Au-Cu-Ag-Mo porphyry deposit, northwestern British Columbia, Canada. In: *Geological Fieldwork 2014*, British Columbia Ministry of Energy and Mines, British Columbia Geological Survey Paper 2015-1, pp. 59-86.
- Foster, D.A., and Hyndman, D.W., 1990. Magma mixing and mingling between synplutonic mafic dikes and granite in the Idaho-Bitterroot Batholith. *Geological Society of America, Memoir*, 174, 347-358.
- Gagnon, J.F., Barresi, T., Waldron, J.W.F., Nelson, J.L., Poulton, T. P., and Cordey, F., 2012. Stratigraphy of the upper Hazelton Group and the Jurassic evolution of the Stikine Terrane, British Columbia. *Canadian Journal of Earth Sciences*, 49, 1027-1052.
- Holbeck, P., 1983. Report on the geology and geochemistry of the Hoodoo West claim group; BC Ministry of Energy and Mines, Assessment Report 12220, 13p. plus maps.
- Irvine, T.N., and Baragar, W.R.A., 1971. A guide to the chemical classification of the common volcanic rocks. *Canadian Journal of Earth Sciences*, 8, 523-548.
- Ishihara, S., 1977. The magnetite-series and ilmenite-series granitic rocks. *Mining Geology*, 27, 293-305.
- Ishihara, S., 1981. The Granitoid Series and Mineralization. *Economic Geology 75th Anniversary Volume*, 458-484.
- Kellett, D. and Joyce, N., 2014. Analytical details of the single- and multicollection $^{40}\text{Ar}/^{39}\text{Ar}$ measurements for conventional step-heating and total-fusion age calculation using the Nu Noblesse at the Geological Survey of Canada. Geological Survey of Canada, Technical Note 8, 27p.
- Kuiper, K.F., Deino, A., Hilgen, F.J., Krijgsman, W., Renne P.R. and Wijbrans, J.R., 2008. Synchronizing rock clocks of Earth history. *Science*, 320, 500-504.
- Kyba, J., and Nelson, J.L., 2015. Stratigraphic and tectonic framework of the Khyber-Sericite-Pins mineralized trend, lower Iskut River, northwest British Columbia: Geological Fieldwork 2014, British Columbia Ministry of Energy and Mines, British Columbia Geological Survey Paper 2015-1, pp. 41-58.
- Lee, J.-Y., Marti, K., Severinghaus, J.P., Kawamura, K., Yoo, H.-S., Lee, J.B., and Kim, J.S. 2006. A redetermination of the isotopic abundances of atmospheric Ar. *Geochimica et Cosmochimica Acta*, 70, 4507-4512.
- Lefebvre, D.V. and Church, B.N., 1996. Polymetallic Veins Ag-Pb-Zn+/-Au, in *Selected British Columbia Mineral Deposit Profiles, Volume 2 - Metallic Deposits*, Lefebvre, D.V. and Höy, T., (Eds.), British Columbia Ministry of Employment and Investment, British Columbia Geological Survey, Open File Report 1996-13, pp. 67-70.
- Lewis, P.D., 2013. Iskut River area geology, northwest British Columbia (104B/08, 09, 10 & part of 104B/01,07,11). *Geoscience British Columbia Report 2013-05*, 3 1:50,000-scale maps, legend and notes, .shp files.
- Lewis, P.D., Toma, A., and Tosdal, R.M., 2001. Metallogenesis of the Iskut River Area, Northwestern British Columbia. University of British Columbia, Mineral Deposits Research Unit, Special Publication Number 1, 337p.
- Logan, J.M., and Koyanagi, V.M., 1994. Geology and mineral deposits of the Galore Creek area (104G/3, 4). British Columbia Ministry of Energy, Mines and Petroleum Resources, British Columbia Geological Survey, Bulletin 92, 95p.
- Logan, J.M., and Mihalynuk, M.G., 2014. Tectonic controls on early Mesozoic paired alkaline porphyry deposit belts (Cu-Au + or - Ag-Pt-Pd-Mo) within the Canadian Cordillera. *Economic Geology*, 109, 827-858.

- Logan, J.M., Drobe, J.R., and McClelland, W.C., 2000. Geology of the Forrest Kerr-Mess Creek area, northwestern British Columbia (NTS 104B/10,15 & 104G/2 & 7W). British Columbia Ministry of Energy and Mines, British Columbia Geological Survey, Bulletin 104, 163p.
- Macdonald, A.J., 1993. Lithostratigraphy and Geochronometry, Brucejack Lake, Northwestern British Columbia. In: Ministry of Energy, Mines and Petroleum Resources, British Columbia Geological Survey, Geological Fieldwork 1992, Paper 1993-1, pp. 315-323.
- Macdonald, A.J., Lewis, P.D., Thompson, J.F.H., Nadaraju, G., Bartsch, R., Bridge, D.J., Rhys, D.A., Roth, T., Kaip, A., Godwin, C.I., and Sinclair, A.J., 1996. Metallogeny of an Early to Middle Jurassic arc, Iskut River area, northwestern British Columbia. *Economic Geology*, 91, 1098-1147.
- Mark, D.F., Stuart, F.M. and de Podesta, M., 2011. New high-precision measurements of the isotopic composition of atmospheric argon. *Geochimica et Cosmochimica Acta*, 75, 7494-7501.
- Markey R.J., Stein, H.J., and Morgan, J.W., 1998. Highly precise Re-Os dating for molybdenite using alkaline fusion and NTIMS. *Talanta*, 45, 935-946.
- Markey R.J., Stein, H.J., Hannah, J.L., Selby, D., Creaser, R.A., 2007. Standardizing Re-Os geochronology: A new molybdenite Reference Material (Henderson, USA) and the stoichiometry of Os salts. *Chemical Geology*, 244, 74-87.
- Mihalynuk, M., Zagorevski, A., and Cordey, F., 2012. Geology of the Hoodoo Mountain area (NTS 104B/14). In: Geological Fieldwork 2011, British Columbia Ministry of Energy, Mines and Natural Gas, British Columbia Geological Survey, Paper 2012-1, pp. 45-67.
- Min, K., Mundil, R., Renne, P.R., and Ludwig, K.R., 2000. A test for systematic errors in $^{40}\text{Ar}/^{39}\text{Ar}$ geochronology through comparison with U/Pb analysis of a 1.1 Ga rhyolite. *Geochimica Cosmochimica Acta*, 64, 73-98.
- Monger, J.W.H., 1977. Upper Paleozoic rocks of the western Canadian Cordillera and their bearing on Cordilleran evolution. *Canadian Journal of Earth Sciences*, 14, 1832-1859.
- Nelson, J.L., and Kyba, J., 2014. Structural and stratigraphic control of porphyry and related mineralization in the Treaty Glacier – KSM – Brucejack – Stewart trend of western Stikinia. In: Geological Fieldwork 2013, British Columbia Ministry of Energy and Mines, British Columbia Geological Survey Paper 2014-1, pp. 111-140.
- Orchard, M.J., 1993. Report On Conodonts And Other Microfossils. Iskut River (104B). 51 Collections By R.G. Anderson 1985-1986, 1989. 224 Unproductive Samples Collected By R.G. Anderson 1984-1991 (Includes Other Map Areas). Geological Survey of Canada, Paleontological Report OF-1993-1, 25p.
- Passchier, C.W., and Trouw, R.A.J., 1998. *Microtectonics*. Springer-Verlag, Berlin Heidelberg, 289p.
- Robb, L., 2005. Introduction to Ore-Forming Processes, Chapter 3: Hydrothermal Ore-Forming Processes, Wiley-Blackwell, United Kingdom, pp. 174-176.
- Roddick, J.C., 1988. The assessment of errors in $^{40}\text{Ar}/^{39}\text{Ar}$ dating. In: Radiogenic Age and Isotopic Studies, Report 2. Geological Survey of Canada, Paper 88-2, pp. 7-16.
- Roddick, J.C., Cliff, R.A., and Rex, D.C., 1980. The evolution of excess argon in alpine biotites - a $^{40}\text{Ar}/^{39}\text{Ar}$ analysis. *Earth and Planetary Science Letters*, 48, 185-208.
- Selby, D., and Creaser, R.A., 2004. Macroscale NTIMS and microscale LA-MC-ICP-MS Re-Os isotopic analysis of molybdenite: Testing spatial restrictions for reliable Re-Os age determinations, and implications for the decoupling of Re and Os within molybdenite. *Geochimica et Cosmochimica Acta*, 68, 3897-3908.
- Sun, S.S., and McDonough, W.F., 1989. Chemical and isotopic systematics of oceanic basalts; implications for mantle composition and processes. Geological Society, Special Publication, 42, 313-345.
- Tipper, H.W., and Richards, T.A., 1976. Jurassic stratigraphy and history of North-central British Columbia. Geological Survey of Canada, Bulletin, 270, 82p.
- Whalen, J., and Frost, C., 2013. The Q-ANOR diagram: A tool for the petrogenetic and tectonomagmatic characterization of granitic suites. Geological Society of America, Abstracts with Programs, 45, 24.
- York, D., 1969. Least-squares fitting of a straight line with correlated errors. *Earth Planetary Science Letters*, 5, 320-324.
- Zagorevski, A., Mihalynuk, M.G., Joyce, N.L., Kellett, D.A., Milidragovic, D., 2015. Characterization of volcanic and intrusive rocks across the British Columbia - Yukon border, GEM 2 Cordillera. Geological Survey of Canada, Open File 7956, 2015; 13 pages, doi:10.4095/297272.